A petrochronological study of Fe Ti oxides in rodingites of the Western Carpathians, Slovakia

Juraj Butek, Damien Dufourcau, Stéphanie Duchene, Oscar Laurent, Michel Gregoire, Ján Spišiak

A petrochronological study of Fe-Ti oxides in rodingites of the Western Carpathians, Slovakia

[1,2] Juraj BUTEK*, [2] Damien DUFOURCAU, [2] Stéphanie DUCHENE, [2] Oscar LAURENT, [2] Michel GRÉGOIRE, [1] Ján SPIŠIAK

[1] Departement of Geography and Geology, Faculty of Natural Sciences, Matej Bel University, Tajovského 40, 97401 Banská Bystrica, Slovakia
[2] Géosciences Environnement Toulouse (GET), CNRS, UPS, IRD, CNES, Université de Toulouse, Observatoire Midi Pyrénées (OMP), 14 Av. E. Belin, 31400 Toulouse, France

*corresponding author: juraj.butek@umb.sk

Highlights

- Fe-Ti rich aggregates occur in rodingites from the Western Carpathians
- The aggregates consist of ilmenite, rutile, titanite and calcite
- Rutile formed by retrograde breakdown of titanite
- Crystallization age of rutile is 102.6 ± 19.9 Ma, consistent with Alpine metamorphism
- Rodingitization took place during exhumation and cooling of an accretionary wedge

Abstract

Rodingitization is the metasomatic transformation of mafic lithologies into rodingite, a Ca-rich and Si-poor rock associated with serpentinized ultramafic bodies. Serpentinization and rodingitization occur simultaneously but it remains challenging to obtain absolute ages on these events in order to identify the geodynamic setting of their formation. In this study, we investigate rodingites from an occurrence in the Western Carpathians with the aim to define the timing of rodingite formation during the tectono-metamorphic evolution of the Carpathian Orogen. The rodingites consist mainly of vesuvianite, diopside, garnet and chlorite. They are noticeably characterized by the presence of Fe-Ti rich aggregates composed of ilmenite, rutile, titanite and calcite. Textural relationships and chemical compositions of the investigated Fe-Ti minerals document their hydrothermal-metamorphic origin. These minerals are characterized by considerable rare earth element (REE) concentrations with prevailing positive Eu anomaly, which presumably derives from the plagioclase-rich protolith of the investigated rodingites. Moreover, the similarity of REE patterns between the analysed phases suggests that the REE concentrations in Fe-Ti minerals are controlled by the immobility and availability of these elements in the system. A particular lamellae texture composed of rutile and calcite originated from titanite destabilization. The titanite destabilization was triggered by cooling, silica leaching and influx of CO_2-rich fluids. In situ U-Pb dating of rutile, which have formed by retrograde breakdown of titanite during rodingitization, yields a crystallization age of 102.6 ± 19.9 Ma. This age is in good agreement with Cretaceous ages of the regional alpine metamorphic evolution reported in the literature and suggests that the rodingitization and serpentinization processes took place during the exhumation and cooling of the accretionary wedge resulting from the closure of the Meliata Ocean.

Keywords: rodingite, rutile, geochemistry, LA-ICP-MS, U-Pb dating, Western Carpathians

1 Introduction

Rodingites represent a specific type of calcium-rich and silica-poor metasomatic rocks consisting of Ca-rich, often hydrated silicate minerals such as garnet, diopside, vesuvianite, epidote-zoisite, chlorite, or prehnite (Li et al., 2004; Schandl et al., 1989). They generally form by hydrothermal alteration of a gabbroic rock enclosed within ultramafic serpentinized lithologies (Koutsovitis, 2017; Li et al., 2017; Pomonis et al., 2008; Tang et al., 2018). The rodingitization and serpentinization processes are typically considered as two concomitant events of the hydrothermal alteration (Honnorez and Kirst, 1975). Ocean floor has been considered to be the most common environment of rodingite formation (Honnorez and Kirst, 1975), yet rodingites can form virtually anywhere along a burial – exhumation path in subduction zone environments (Koutsovitis et al., 2013; Li et al., 2010, 2007; Rogkala et al., 2022). In order to reliably identify the geodynamic setting of serpentinite and rodingite formation, solid chronological data can provide useful constraints.

However, serpentinized ultramafic lithologies are generally difficult to date because of their monotonous mineralogy not allowing the use of conventional radiometric dating methods, perhaps only with the exeption of the recently emerging approach by the (U-Th)/He dating of magnetite (Schwartz et al., 2020). Researchers thus often focus either on the reaction zones between serpentinites and their surrounding lithologies or on rodingites with the objective to find minerals suitable for dating. Successful chronological data have been obtained on zircon (Dubińska et al., 2004; Hu and Santosh, 2018; Li et al., 2010), perovskite (Li et al., 2014; Shen et al., 2016), and garnet (Haws et al., 2021). In this study, we present the potential of rutile in-situ U-Pb dating for the first time to constrain the age of hydrothermal alteration of a mafic-ultramafic system.

Fe-Ti oxides (rutile, ilmenite, titanomagnetite, ulvospinel or magnetite) are common accessory minerals in many metamorphic, magmatic and also detrital rocks. Rodingites are no exception and often contain minor amounts of these phases, mainly rutile and ilmenite (Butek et al., 2022; Koutsovitis et al., 2018, 2013; Laborda-López et al., 2018; Nishiyama et al., 2017). Any attempt to date the metasomatic process with rutile U-Pb geochronology requires a good understanding of 1) the relationship between fluid circulation and Fe-Ti oxide phase equilibria and 2) behaviour of the chemical and isotopic systems during and after mineral crystallization. However, whereas reactions between rutile and other Ti-bearing minerals are well documented in felsic natural (Angiboust and Harlov, 2017; e.g. Broska et al., 2007; Henze et al., 2023; Schirra and Laurent, 2021) or experimental (Janssen et al., 2010; Lucassen et al., 2012) systems, they have been so far rarely described in rodingites or in mafic rocks generally (Liou et al., 1998; Mohammad and Maekawa, 2008).

This study focuses on rodingitized gabbroic rocks associated with an ophiolite fragment in the Western Carpathians, the Bôrček serpentinite body, which has been presented in detail by Butek et al. (2022). Through a combination of textural analysis and U-Pb LA-ICPMS dating, we discuss the reaction scheme of Ti-rich minerals during rodingitization, and demonstrate that hydrothermal rutile can provide a chronological record of the Cretaceous metasomatism and can help to discuss the timing of rodingite formation in the framework of the regional geodynamical evolution.

2 Geological setting

The Central Western Carpathians are delimited by two latitudinally oriented suture zones corresponding to the closure of two oceanic domains: I) in the south, the Meliata (Meliata-Hallstatt) Ocean with lifetime from the Middle Triassic to the Upper Jurassic (Kozur, 1991) and II) in the north, the Penninic-Vahic Ocean with lifetime from the Middle Jurassic to the Early Tertiary (Plašienka, 2018). Southern parts of the Central Western Carpathians (Fig 1a, b) are dominated by two thick-skinned units (Veporicum and Gemericum) and several north-vergent thin nappe units (Meliaticum, Turnaicum and Silicicum) emplaced during the alpine collision-obduction processes. The suture zone of the Meliata Ocean is affected by crustal-scale faults and buried under younger units and sediments, therefore, it is not recognized on the surface (Fig. 1c).

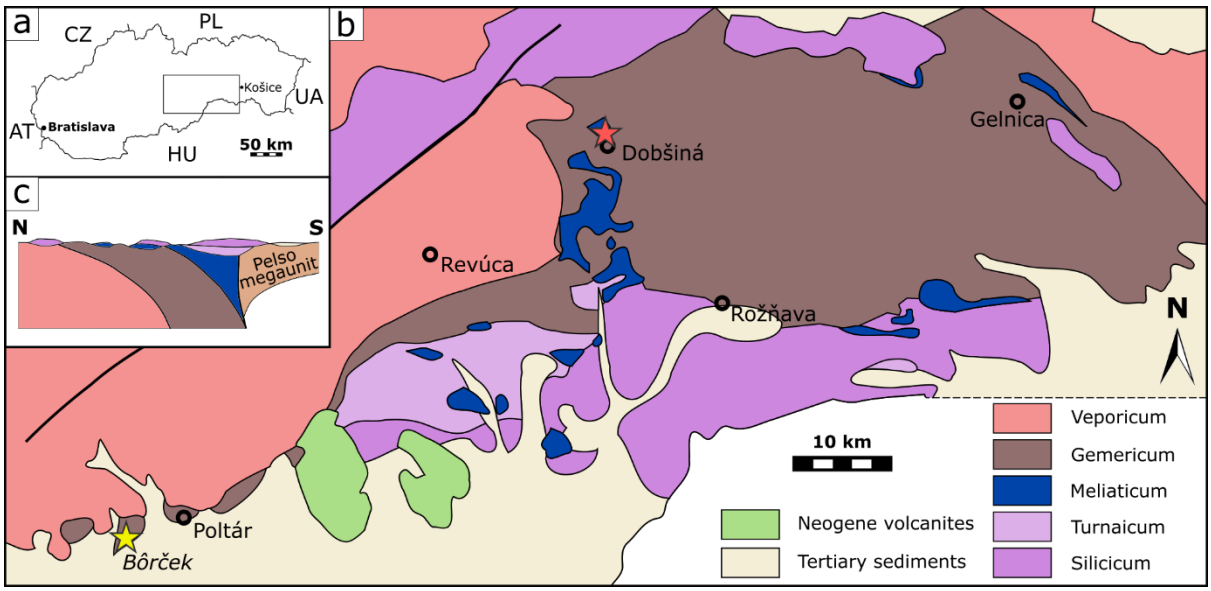

Fig. 1. *a) Localization of the southern parts of the Western Carpathians in Slovakia. The rectangle delineates the region displayed in b. b) Simplified geological map of the Veporic-Gemeric zone in the Western Carpathians (modified after "Geologická mapa Slovenska [online], ŠGÚDŠ," 2013). The yellow star marks the investigated serpentinite and rodingite occurrence (see also Butek et al. 2022). The red star marks the Dobšiná rodingite occurrence (Butek et al., 2021) where dating of perovskite formation allowed to constrain the age of serpentinization processes (Li et al. 2014). c) Simplified geological north-south oriented cross-section sketch of the presented region (adopted from Plašienka 2018).*

The Veporicum represents an extensively exhumed unit consisting of a pre-alpine crystalline basement formed of Paleozoic magmatic and high-grade metamorphic rocks of the Variscan origin. The basement is locally covered with sedimentary sequences (Permian – Upper Triassic) affected by greenschist facies metamorphism. The Gemericum consists of mostly low-grade metavolcano-sedimentary basement (Lower Paleozoic) locally intruded by Permian granitic rocks. Sedimentary cover (Pennsylvanian – Lower Triassic) is represented by variegated low-grade metasedimentary rocks including terrestrial clastics, carbonates, phyllites and basic volcanoclastics. The Meliaticum consists of heterogeneous rock complexes. In its basal position, it is formed of marbles and high-pressure low-temperature metamorphic rocks including glaucophanites, which evidence the subduction environment. Furthermore, the Meliaticum comprises ophiolite-bearing mélanges of Triassic carbonates, radiolarites and volcanic rocks, found within grey shales and radiolarite beds of the

Jurassic age. The closure of the Meliata oceanic domain resulted in the north-vergent tectonic transport of rock complexes, including the uppermost nappe units Turnaicum and Silicicum. The Turnaicum (Late Carboniferous – Late Triassic) is distinguished by only slightly metamorphosed deep-water sedimentary rocks, dominantly Triassic grey nodular limestones and grey shales. The Silicicum (Upper Permian – Early Cretaceous) consists mainly of unmetamorphosed Triassic shallow-water fossil-rich carbonate sedimentary rocks. The Pelso megaunit (Fig. 1c) is exposed mostly in isolated mountains in northern Hungary and comprises unmetamorphosed Paleozoic and Mesozoic complexes that form a south-directed fold-and-thrust belt (Plašienka, 2018 and references therein).

Occurrences of ultramafic rocks in the southern part of the Western Carpathians can be distinguished into three groups: 1) serpentinite bodies occurring in the Gemericum and associated with high grade metamorphic rocks represented by gneisses and amphibolites, the so-called Klátov unit (Hovorka et al., 1990). These serpentinized ultramafic rocks consist of antigorite and their origin is ascribed to a (pre-)Variscan subduction zone (Faryad et al., 2020; Radvanec et al., 2017). 2) Serpentinite bodies associated with Triassic sedimentary-mélange complexes belonging to the Meliaticum. Chrysotile and lizardite predominate in these bodies, while antigorite is rare (Hovorka et al., 1980). Their origin is ascribed to obduction processes during the closure of the Triassic-Jurassic Meliata Ocean in the Jurassic period (Ivan, 2002; Plašienka et al., 2019). 3) Serpentinite bodies in association with low grade metasediments (Gemericum) of Paleozoic age. These serpentinites are composed dominantly of antigorite and their age and provenance remain uncertain (Hovorka et al., 1985, 1983). The investigated rodingites, sampled at the Bôrček locality, about 5 km south-west from Poltár (Fig. 1b), are representative of the third group. Rodingites are hosted by intensively serpentinized ultramafic bodies tectonically incorporated into Gemeric metasediments of Carboniferous age. For more details on the regional geology and the outcrop, the reader is referred to Butek et al. (2022).

3 Methodology

Following conventional petrographic observations, back scattered electron (BSE) imaging and wavelength-dispersive spectroscopy (WDS) microprobe analyses of the investigated Fe-Ti minerals were performed on thin sections using a JEOL JXA-8530FE instrument operated at the Earth Science Institute of the Slovak Academy of Science, Banská Bystrica, Slovakia. An accelerating voltage of 15 kV, a current of 20 nA, and a spot size of 2-5 µm were used for the major element quantification.

Minerals were analysed on thin sections for U-Pb dating and trace element concentration by laser ablation-inductively coupled plasma-mass spectrometry (LA-ICP-MS). The analyses were carried out at the Service ICP-MS of Observatoire Midi-Pyrénées (OMP), Toulouse, France, using a NWRfemto (Elemental Scientific Instruments) solid-state femtosecond laser ablation system operated in UV mode (257 nm wavelength) attached to an Element XR (Thermo) sector-field ICP-MS.

Two different sequences were run, the first one optimised for trace element determination but with U-Pb isotopic ratios screened to evaluate the dating potential; and the second one optimised for U-Pb dating alone. In both cases, we have used a laser repetition rate of 7 Hz, spot diameter of 30 µm and fluence of ca. 2.8 $J.cm^{-2}$. Ablation was performed in the built-in, dual-volume ablation cell (< 1 cm^3 effective volume) fluxed with carrier gas consisting of ca. 0.6 $L.min^{-1}$ He. Make-up gas consisting of ca. 0.9 $L.min^{-1}$ Ar was admixed downstream of the ablation cell. Each analysis consisted in 20 s of background acquisition followed by 30 s of sample ablation and 10 s washout. No signal smoothing device was used. The ICP-MS instrument was optimized for maximum sensitivity on Th and U while

keeping low the production of oxides ($^{254}UO^+/^{238}U^+ \leq 0.1$ %) and the Th/U ratio as close to 1 as possible (on NIST SRM610 glass). The list of acquired masses and corresponding dwell times for the two setups, as well as further details about the method and instrumentation, are provided in the Table S1.

For U-Pb dating, the raw signals were processed offline with the Igor Pro Iolite v2.5 software (Hellstrom et al., 2008), using the VizualAge data reduction scheme (Petrus and Kamber, 2012). Background-subtracted intensities were used to calculate isotope ratios, which were corrected for laser-induced Pb/U fractionation (after Paton et al., 2010), mass discrimination and drift through the analytical session by conventional standard-sample bracketing, against rutile reference material R10 (Luvizotto et al., 2009). No common Pb correction was carried out. Rutile reference materials R13 (Schmitt and Zack, 2012) and WOD-B (Schirra and Laurent, 2021) were used as validation standards. The obtained ages for all secondary standards are accurate within less than 1 % (Tab. S1).

For trace elements, the raw signals were processed using the GLITTER software (Griffin et al., 2008). Trace element concentrations were calibrated against the NIST SRM610 glass reference material (Jochum et al., 2011) using the TiO_2 content (measured by WDS analyses) as internal standard for relative sensitivity correction (rutile – 99.5 wt.%, ilmenite – 52.5 wt.%, titanite – 39 wt.%). Rutile reference material R10 (Luvizotto et al., 2009) was used as a validation standard. The trace element concentrations obtained for R10 are accurate within < 10 % relative for Zr, Nb, Sb, Hf; within 10-15 % relative for V, Mo and Ta; and within 20-25 % relative for W and U (Tab. S2). Data plotting and age calculations were performed using the IsoplotR toolbox (Vermeesch, 2018).

4 Results

4.1 Petrography

The investigated samples represent a product of intense rodingitization of a gabbroic protolith (Butek et al., 2022). They consist predominantly of vesuvianite, diopside, hydrated garnet and titanite. Two generations of garnet and vesuvianite are present, the first ones resulting from a pervasive fluid circulation, and the second ones crystallizing mostly within veins or reaction rims. Minor minerals are represented by epidote, chlorite, calcite and Fe-Ti oxides. The latter are the main focus of this study.

Fe-Ti oxides (rutile and ilmenite) occur in irregularly distributed aggregates within silicate minerals. The size, shape and modal composition of these oxide-rich domains are highly variable. Micrometric oxide grains were observed but locally the aggregates can reach up to 5 mm (Fig. 2) (see also Fig. 3 in Butek et al., 2022). The edges of the aggregates are defined either by sharp contact with a vesuvianite or chlorite vein, or by an irregular, about 100 µm thick reaction rim typically consisting of titanite ± garnet. The mineral composition of the oxide-rich aggregates is dominated by rutile, ilmenite, titanite and calcite. The modal proportion of rutile and ilmenite varies not only between samples, but also between individual aggregates within one sample. Some aggregates consist solely of ilmenite (without rutile) but the majority is characterized by roughly equal amounts of these two phases (Fig. 3a, b). Aggregates dominated by rutile are scarce.

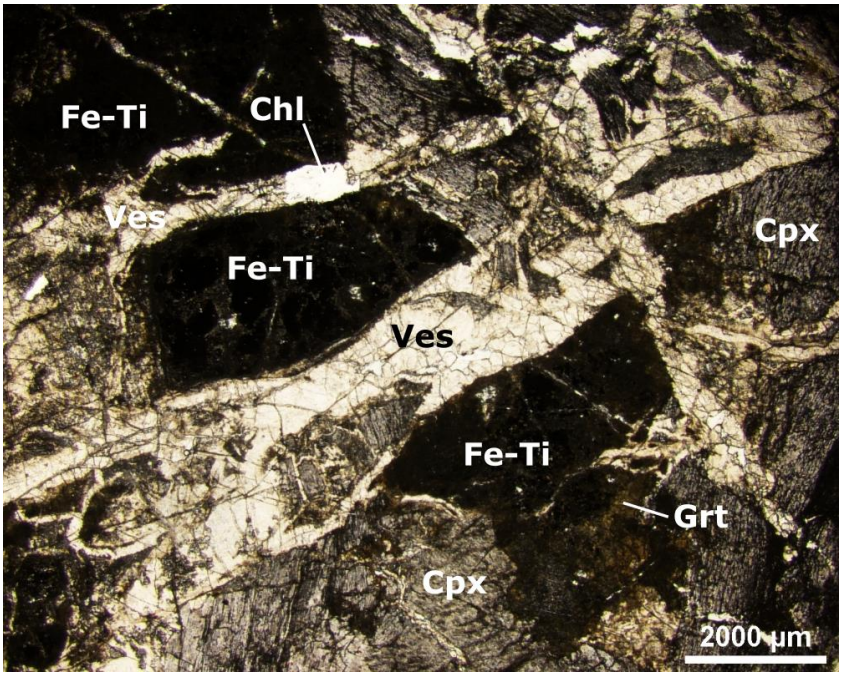

Fig. 2. *Photomicrograph of the relationships between main rodingite minerals (vesuvianite, clinopyroxene, garnet) and Fe-Ti oxide rich aggregates (‚Fe-Ti') consisting of ilmenite + rutile + titanite ± calcite (plane-polarized light, sample FBR57). Mineral abbreviations are after Warr (2021).*

Ilmenite occurs as altered xenomorphic grains of variable size. It can occur as seemingly single crystals reaching several hundreds µm (Fig. 3c) but more commonly it is irregularly dispersed within titanite matrix (Fig. 3b). It typically occurs in close association with rutile often forming fine intergrowth at micrometric scale (Fig. 3b). Locally, ilmenite forms a rim around rutile (Fig. 3d, e).

Rutile, identified both from optical properties and by microRaman measurements (Fig. S1), occurs in two distinguishible forms. The first type, denoted rutile I, forms cores enclosed within ilmenite (Fig. 3d, e). Occurrence of this rutile type is restricted to large Fe-Ti-oxide aggregates. The second type of rutile, denoted rutile II, is significantly more abundant than rutile I. Like ilmenite, it typically occurs as xenomorphic grains dispersed within titanite matrix but hipidiomorphic prismatic crystals were also locally observed. Contrary to rutile I, rutile II is everywhere associated with calcite (Fig. 3d). Dispersed mixed rutile II + calcite grains within titanite locally form an alteration rim around ilmenite (Fig. 3c). The most striking feature of rutile II occurrence is a specific oriented texture consisting of alternance of rutile and calcite (± ilmenite) lamellae (Fig. 3b). These lamellae reach up to 50 µm in width and frequently cover large areas in oxides-rich aggregates. It is worth to note that despite the fact that ilmenite seems to replace rutile in these lamellae, locally they consist exclusively of rutile and calcite. Furthermore, rutile occurs as fine acicular crystals in ilmenite although this texture is rare (Fig. 3f).

Calcite occurs in close spatial association with rutile II, whether in the form of the oriented lamellae or irregularly dispersed grains within titanite matrix. It is worth to emphasize that calcite does not occur in association with rutile I (Fig. 3d, e).

Titanite represents a uniform matrix of the areas rich in oxides. Since the titanite matrix encloses all other minerals and all described textures, titanite seemingly replaces Fe-Ti oxides (Fig. 3b, e). Titanite also rims the oxides-rich aggregates, although the outer parts of the rim are commonly formed by andraditic garnet. Titanite and garnet frequently occur in micrometric intergrowths (Fig. 3g).

Perovskite was infrequently identified as small isolated grains (< 10 µm) surrounded by titanite (Fig. 3g) or as tiny inclusions in rutile or ilmenite (Fig. 3c). The oxides-rich aggregates are characterized also by seldom occurrence of some other accessory phases rarely exceeding 10 µm in size. They are represented mainly by sulfides such as chalcopyrite, polydymite, millerite, bornite and pyrite. Several grains of Zr-bearing minerals (zircon, baddeleyite and zirconolite) and apatite were also identified (Fig. 3g).

4.2 Mineral chemistry

Ilmenite displays a relatively homogeneous composition characterized by slight variations of MgO (1 – 2 wt.%) and MnO (2.5 – 5 wt.%) (Tab. 1). The average total rare earth elements (REE) concentration in ilmenite is around 3 ppm and the chondrite normalized spectra commonly displays a slightly U-shaped pattern with pronounced positive Eu anomaly (Fig. 4). Considering high field strength elements (HFSE), ilmenite contains 6 ppm of Nb, 2 ppm of Ta, 187 ppm of Zr and 4 ppm of Hf, in average (Tab. 2).

Both rutile I and rutile II are characterized by ca. 0.5 wt.% of FeO. However, there are systematic differences between chemical compositions of the two rutile generations. Rutile II contains ca. 0.5 wt.% of CaO which is absent in rutile I (Tab. 1). Furthermore, rutile II displays higher REE concentration (7 ppm in average) with a slightly LREE-enriched chondrite normalized pattern and positive Eu anomaly, compared to rutile I whose REE content is generally near the detection limit (Fig. 4). Considering HFSE, rutile II contains slightly less Zr (211 ppm) and Hf (4 ppm) in average, than rutile I (Zr: 409 ppm; Hf: 12 ppm). Rutile II also displays higher W (285 ppm), Sb (236 ppm), and lower V (1627 ppm), Cr (128 ppm) and Sn (0.6 ppm) in average, than type I rutile (W: 37 ppm; Sb: 26 ppm; V: 2710 ppm; Cr: 199 ppm and Sn: 5.9 ppm) (Fig 5).

Electron microprobe analyses allowed to detect also a chemically heterogeneous phase with major element compositon resembling pseudorutile (Fig. 3h). This phase consists mainly of TiO_2 (62 – 66.4 wt.%) and Fe_2O_3 (20.9 – 22.8 wt.%) (Tab. 1), however, some other elements are present in significant concentrations, most notably: V_2O_3 (2.4 – 6.2 wt.%), CaO (2.6 – 5.6 wt.%) and SrO (0.3 – 2.8 wt.%). Moreover, low sum in some analyses of this mineral indicates incorporation of a non-measurable component, presumably H_2O.

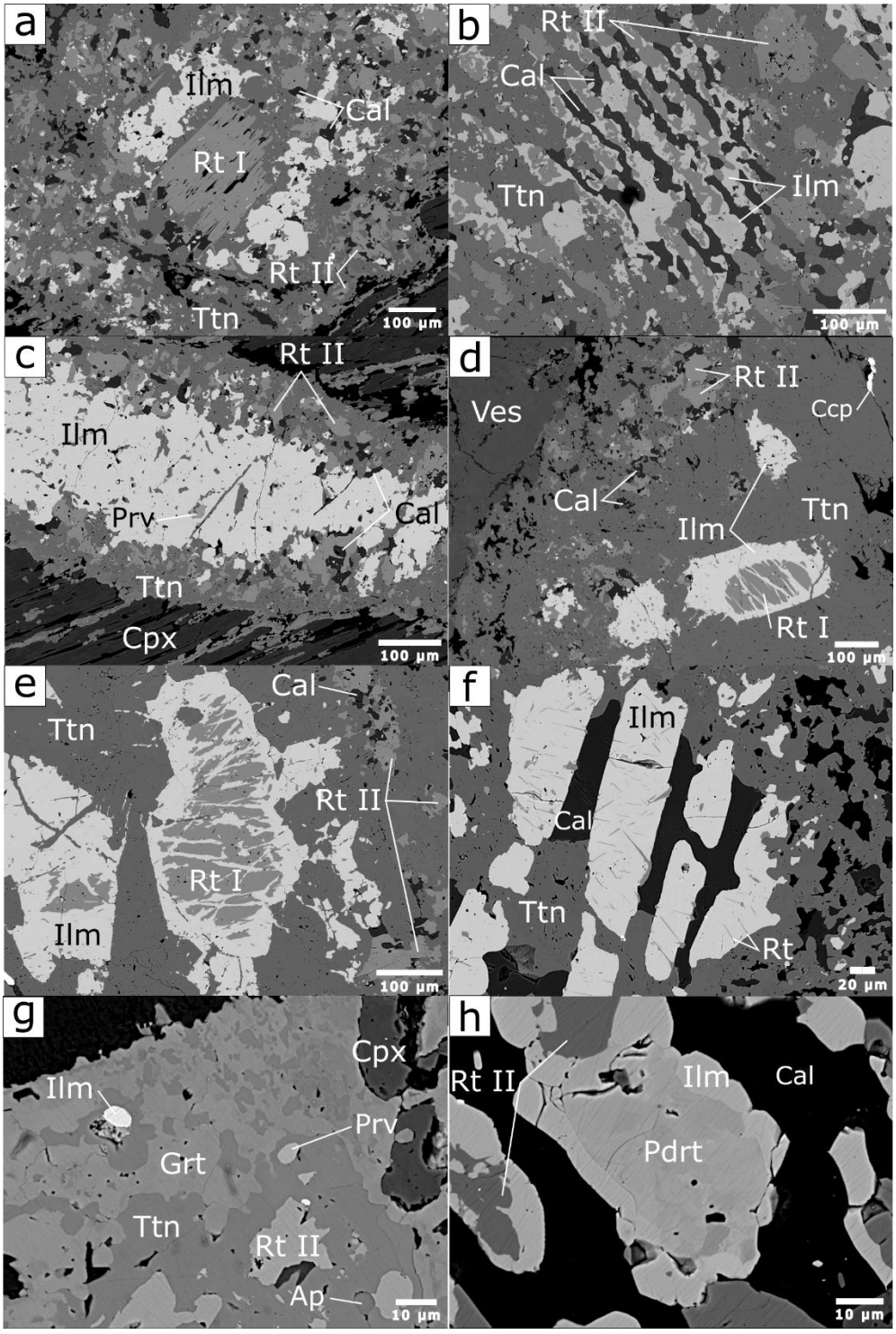

Fig. 3. *Back-scattered Electron (BSE) images of the key rock textures and minerals (sample label in brackets). a) Crystal of rutile I surrounded by the dominant texture of dispersed ilmenite, rutile II and calcite in a titanite matrix (FBR-64). b) Rutile II + calcite lamellae texture replaced by ilmenite and enclosed by the titanite matrix (FBR-56). c) Ilmenite grain showing an alteration rim consisting of titanite, rutile II and calcite. Note also the perovskite occurrence (FBR-64). d), e) Contrasting two types of rutile occurences: rutile I forms a core and is uniformly rimmed by ilmenite. Rutile II is more dispersed and occurs everywhere in association with calcite. The matrix is represented by titanite (FBR-57). f) Acicular rutile (undefined generation) occurring in ilmenite (FBR-56). g) Fe-Ti oxides (including perovskite) surrounded by titanite. At outer rim of the aggregates, titanite forms fine-grained intergrowths with garnet (FBR-57). h) Detail of heterogeneous pseudorutile rimmed by homogeneous ilmenite (FBR-56). Mineral abbreviations are after Warr (2021).*

Table 1 *Selected major oxides composition (wt.%, determined by EMPA) and structural formulas of the investigated rodingite minerals. Additional analyses are available in the Table S3.*

mineral	**Rt I**	**Rt I**	**Rt II**	**Rt II**	**Ilm**	**Ilm**	**Ilm**	**Pdrt**	**Pdrt**	**Pdrt**	**Prv**	**Prv**	**Prv**	**Ttn**	**Ttn**	**Ttn**
sample	FBR-57	FBR-57	FBR-64	FBR-56	FBR-64	FBR-64	FBR-57	FBR-56	FBR-56	FBR-56	FBR-57	FBR-57	FBR-57	FBR-64	FBR-56	FBR-57
SiO_2	-	0.03	0.02	-	0.01	-	-	-	-	-	-	-	0.02	30.07	30.70	30.49
TiO_2	97.33	98.71	98.60	97.42	51.89	52.87	50.11	63.76	65.10	65.03	60.22	59.58	59.90	40.47	40.68	39.31
ZrO_2	0.09	0.05	n.a.	0.05	n.a.	n.a.	0.06	n.a.	0.29	0.16	-	-	0.02	n.a.	0.07	-
Al_2O_3	-	0.02	0.02	0.01	0.02	-	0.02	0.92	0.78	0.61	-	0.01	0.01	0.68	0.46	0.61
Cr_2O_3	0.01	0.01	-	0.07	-	-	-	0.40	0.15	0.12	0.00	0.00	0.04	0.03	0.02	0.02
V_2O_3	0.79	0.84	0.90	0.90	0.40	0.34	0.30	**3.79**	**2.45**	**4.25**	0.28	0.32	0.33	0.68	0.24	0.31
$FeO_{tot.}$	0.51	0.41	0.36	0.51	41.13	40.47	40.38	19.60	20.27	19.12	-	0.82	0.08	0.27	0.23	0.14
MnO	0.08	0.05	0.01	0.01	4.54	4.75	4.35	1.03	0.68	0.72	0.02	0.07	-	0.04	-	0.03
MgO	-	-	0.01	-	1.95	1.89	1.65	0.23	0.20	0.18	0.02	0.01	0.02	-	-	-
CaO	0.04	0.01	**0.67**	**0.54**	0.04	0.16	0.10	**3.41**	**5.10**	**4.10**	37.23	39.82	37.47	26.92	27.43	27.73
SrO	0.05	-	0.03	0.06	0.04	-	-	**2.18**	**1.01**	**2.66**	-	-	0.00	-	0.11	0.13
Na_2O	0.04	0.05	n.a.	0.04	n.a.	n.a.	-	n.a.	0.05	0.07	-	0.01	0.01	n.a.	0.01	0.02
Ta_2O_5	-	-	n.a.	-	n.a.	n.a.	-	n.a.	0.12	0.07	0.04	-	-	n.a.	0.10	-
Nb_2O_5	0.10	-	n.a.	-	n.a.	n.a.	0.03	n.a.	0.05	0.00	0.01	-	0.03	n.a.	0.07	-
Total	99.04	100.16	100.62	99.61	100.01	100.47	97.00	95.32	96.25	97.10	97.82	100.62	97.93	99.15	100.12	98.78
	recalculated atoms per formula unit															
Si^{4+}	-	0.00	0.00	-	0.00	-	-	-	-	-	-	-	0.00	0.99	1.00	1.01
Ti^{4+}	0.99	0.99	0.99	0.98	0.97	0.98	0.97	3.26	3.27	3.28	1.04	1.01	1.03	1.00	1.00	0.98
Zr^{4+}	0.00	0.00		0.00			0.00		0.01	0.01	-	-	0.00		0.00	-
Al^{3+}	-	0.00	0.00	0.00	0.00	-	0.00	0.07	0.06	0.05	-	0.00	0.00	0.03	0.02	0.02
Cr^{3+}	0.00	0.00	-	0.00	-	-	-	0.02	0.01	0.01	0.00	0.00	0.00	0.00	0.00	0.00
V^{3+}	0.01	0.01	0.01	0.01	0.01	0.01	0.01	0.17	0.11	0.19	0.00	0.00	0.01	0.01	0.01	0.01
Fe^{3+}	0.01	0.00	0.00	0.01	0.05	0.03	0.06	1.11	1.13	1.07	-	-	-	0.01	0.01	0.00
Fe^{2+}	-	-	-	-	0.80	0.81	0.81	-	-	-	-	0.02	0.00	-	-	-
Mn^{2+}	0.00	0.00	0.00	0.00	0.10	0.10	0.09	0.06	0.04	0.04	0.00	0.00	-	0.00	-	0.00
Mg^{2+}	-	-	0.00	-	0.07	0.07	0.06	0.02	0.02	0.02	0.00	0.00	0.00	-	-	-
Ca^{2+}	0.00	0.00	0.01	0.01	0.00	0.00	0.00	0.25	0.37	0.29	0.91	0.96	0.92	0.95	0.96	0.98
Sr^{2+}	0.00	-	0.00	0.00	0.00	-	-	0.09	0.04	0.10	-	-	0.00	-	0.00	0.00
Na^{+}	0.00	0.00	-	0.00			-		0.01	0.01	-	0.00	0.00		0.00	0.00
$\Sigma_{cations}$	1.00	1.00	1.01	1.01	2.00	2.00	2.00	5.05	5.06	5.06	1.96	1.99	1.96	2.99	2.99	3.00

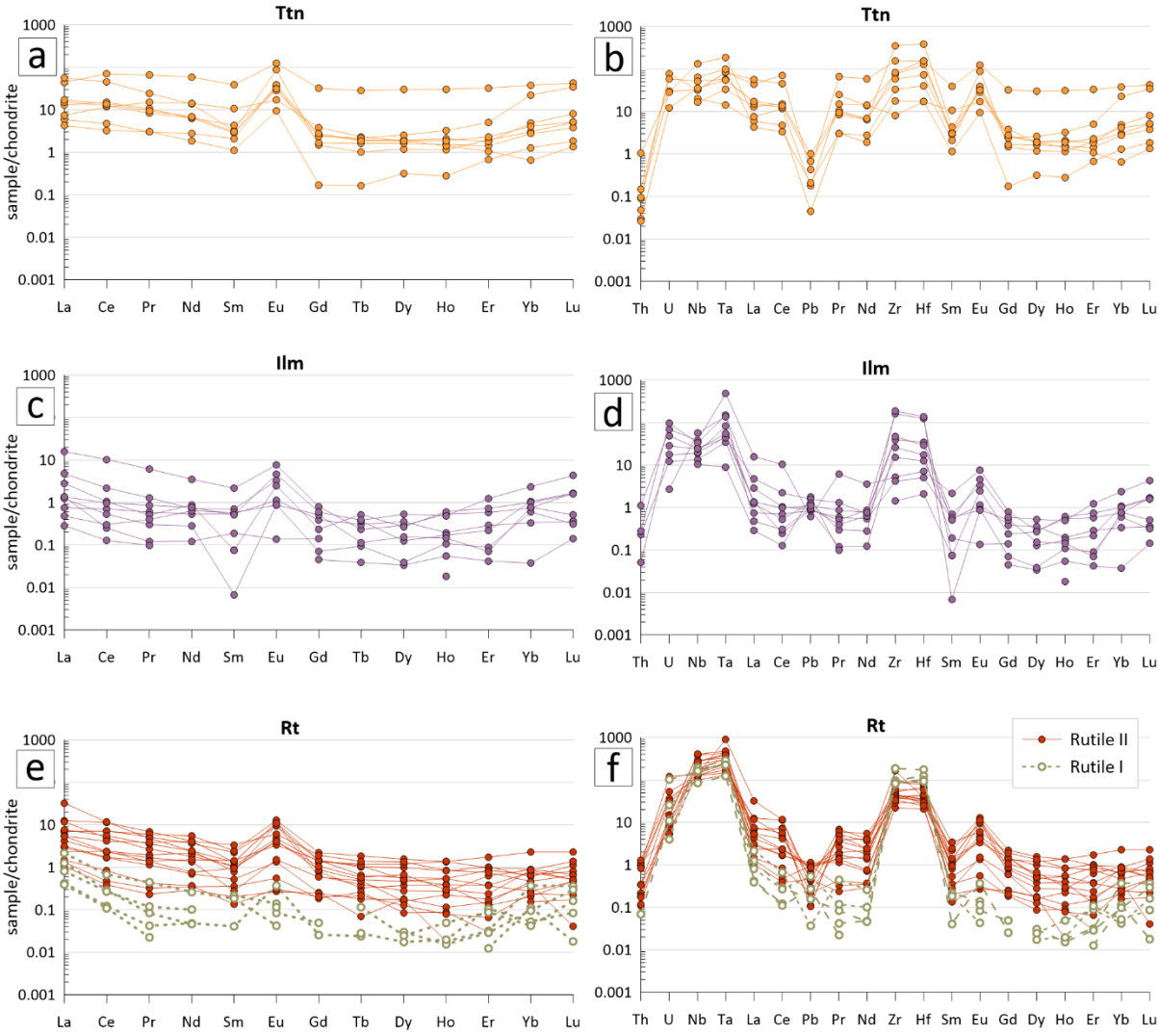

Fig. 4. *Chondrite-normalized REE and trace element spider diagrams for the investigated Ti-minerals (chondrite values from McDonough and Sun 1995). a, b) titanite. c, d) ilmenite. e, f) two generations of rutile. Each pattern represents a single LA-ICP-MS analysis. Raw data are available in the Table S4.*

Titanite displays variable contents of TiO_2 (36.5 – 40.8 wt.%) and CaO (26.5 – 28.2 wt.%). Its composition is further characterized by low FeO (< 0.7 wt.%), Al_2O_3 (< 1.3 wt.%) and MgO (< 0.1 wt.%) contents. No systematic zonation was observed. The average total REE concentration in titanite is 36 ppm and the chondrite normalized spectra displays a relatively flat pattern with pronounced positive Eu anomaly (Fig. 4). Considering HFSE, titanite contains 12 ppm of Nb, 1 ppm of Ta, 372 ppm of Zr and 13 ppm of Hf, in average.

The REE spectra of all the investigated minerals (except rutile I) are very similar in shape and always display the positive Eu anomaly. Furthermore, the concentrations of HFSE are generally low and also comparable in all the investigated minerals. Pb, U and Th concentrations are consistently very low and rarely reach 4, 0.2 and 0.04 ppm, respectively (Tab. 2). Ilmenite, titanite, rutile I and also rutile II display a subchondritic Nb/Ta ratio (in average 7.5, 12.3, 12.6, and 12.3, respectively).

Calcite occurring in association with rutile II is chemically pure and homogeneous, only FeO reaches 0.4 wt.% while MgO content is near the detection limit (< 0.09 wt.%).

Table 2 *Selected trace element composition of the investigated Ti minerals (values in ppm, determined by LA-ICP-MS). Additional analyses are available in the Table S4.*

mineral	**Rt I**	**Rt I**	**Rt II**	**Rt II**	**Ilm**	**Ilm**	**Ttn**	**Ttn**
sample	FBR-57	FBR-57	FBR-57	FBR-57	FBR-57	FBR-57	FBR-57	FBR-57
Sc	29.52	34.44	42.76	39.65	108.15	71.15	35.43	38.15
V	2749.44	2851.22	1431.88	1554.89	615.74	939.86	1555.19	1265.56
Cr	175.25	213.05	102.68	142.29	29.68	57.65	25.65	82.17
Co	1.04	13.11	12.24	1.29	89.7	38.14	1.84	-
Ni	10.64	76.93	23.44	3.78	251.58	122.05	10.68	-
Cu	3.73	3.08	2.89	2.32	0.78	1.35	1.92	1.6
Zn	17.62	53.03	19.7	3.83	194.38	113.15	6.46	4.36
Y	0.072	0.08	0.266	0.82	0.45	0.161	1.24	0.61
Zr	345.96	308.39	154.92	136.8	616.66	301.23	287.48	67.45
Nb	20.11	45.69	44.23	42.07	7.93	19.08	7.68	4.83
Mo	0.048	0.22	0.203	0.002	0.82	0.49	0.097	0.1
Sn	4.79	7.29	1.13	1.13	0.31	1.87	6.34	3.23
Sb	9.4	49.82	468.42	371.6	14.59	14.34	1.9	3.4
La	0.093	0.51	0.69	1.81	0.67	0.217	13.32	1.38
Ce	0.067	0.412	1.02	3.4	0.64	0.24	27.9	2.91
Pr	0.002	0.041	0.105	0.33	0.047	0.0229	2.28	0.281
Nd	-	0.12	0.32	1.11	0.4	0.071	6.21	0.85
Sm	0.032	0.027	0.078	0.197	0.011	0.0079	0.48	0.167
Eu	0.008	0.002	0.075	0.63	0.14	0.041	4.91	0.53
Gd	-	-	0.05	0.29	0.047	0.02	0.29	0.034
Tb	-	0.004	0.003	0.024	0.019	0.006	0.037	0.006
Dy	0.007	0.006	0.044	0.140	0.066	0.074	0.293	0.078
Ho	0.001	0.003	0.006	0.030	0.033	0.003	0.062	0.015
Er	0.005	0.014	0.024	0.136	0.118	0.025	0.308	0.107
Tm	0.000	-	0.005	0.013	0.019	0.015	0.067	0.018
Yb	0.016	0.007	0.075	0.106	0.161	0.063	0.492	0.206
Lu	0.007	0.004	-	0.020	0.039	0.011	0.123	0.045
Hf	10.27	10.39	4.38	4.66	12.72	6.46	13	1.78
Ta	1.69	3.06	4.18	3.21	2.03	1.67	1.14	0.194
W	17.97	8.79	243.7	237.91	4.61	1.26	0.72	2.25
Pb^{204}	0.66	0.09	2.78	1.68	2.18	2.09	-	0.11
Th^{232}	-	-	0.006	0.003	0.008	-	0.003	0.001
U^{238}	0.02	0.01	0.01	0.02	0.18	0.06	0.10	0.01

4.3 U-Pb dating

The first LA-ICP-MS analytical session performed on ilmenite, rutile and titanite, aimed at trace element quantification but including screening of U-Pb isotopes for dating, showed that only rutile II of sample FBR-57 was rich enough in U to have a potential for dating, whereas all other minerals returned concentrations close to the limit of detection. Rutile II from this sample was therefore the main target for the second U-Pb dating LA-ICP-MS session. We have pooled 22 rutile analyses from

the first session and 153 from the second one to determine a lower intercept date. The acquired U-Pb data, calculated ages and uncertainties of single analyses are available in the Table S5.

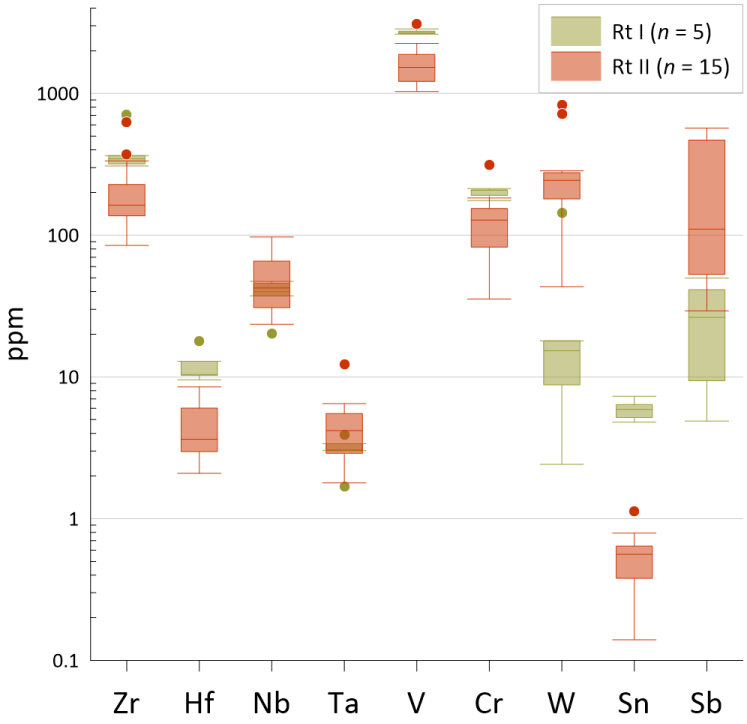

Fig. 5. *Box and whisker plots for HFSE and selected trace element concentrations in the two types of rutile. The box represents the interquartile range; the bar inside the box represents the median; and the whiskers represent the 95% confidence interval. Outliers are represented by the dots of respective colour. Both rutile types show relatively low HFSE concentrations but systematic differences can be noticed in Zr, Hf, V, Cr, W, Sn and Sb. Raw data are available in the Table S4.*

The small size of rutile II and its micrometric overgrowths with ilmenite, titanite and/or calcite imply a probable contamination in the majority of rutile dating analyses (Fig. S2). However, since these surrounding minerals do not have significant U and hence radiogenic Pb concentrations, the contamination would only result in dragging the data towards the common Pb end-member. Altogether, the data define a sub-linear trend in the reverse Concordia diagram. The lower intercept date obtained from rutile II grains of the second analytical session is 99.7 Ma ± 20.5 (2σ; n = 153; MSWD = 0.83). The combination with the rutile II analyses from the first session yields a within-uncertainty identical date, yet slightly more precise, of 102.6 ± 19.9 Ma (2σ; n = 175; MSWD = 0.87; Fig. 6). The obtained Pb isotopic composition ($^{207}Pb/^{206}Pb$ = 0.793 ± 0.004) is consistent with the expected composition of terrestrial Pb at this age (Stacey and Kramers, 1975). We thus interpret this trend as reflecting a mixing between initial (common) Pb and radiogenic Pb and therefore the lower intercept date as the crystallization age of rutile II.

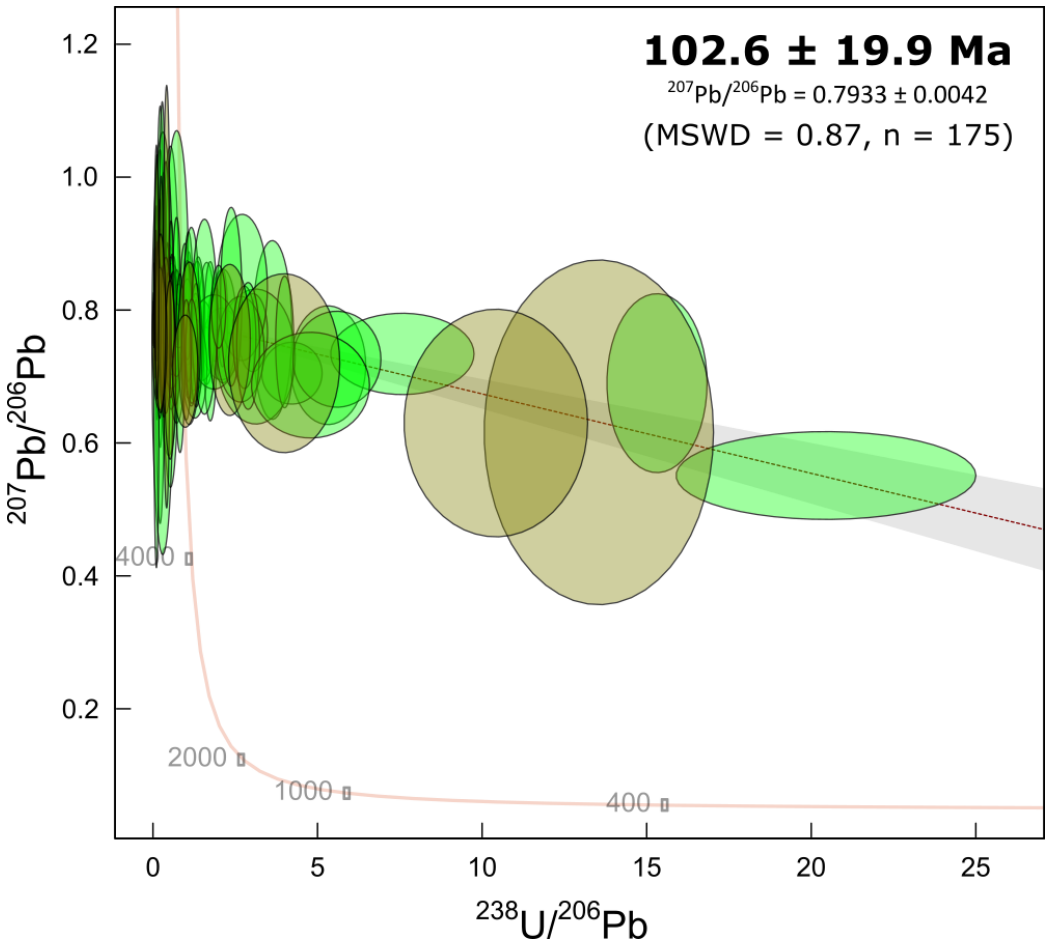

Fig. 6. *Tera-Wasserburg concordia diagram of the U-Pb rutile II dating from Bôrček rodingites, generated with IsoplotR (Vermeesch 2018). The first and the second LA-ICPMS runs (see methodology) are represented by khaki and green colour, respectively. The average age, analytical uncertainty (2σ), and MSWD are given collectively for all analyses. Respective data for each analysis are available in the Table S5.*

5 Discussion

5.1 Significance of trace element concentrations in Fe-Ti oxides

Despite the fact that the measured trace element concentrations in rutile and ilmenite are prone to analytical contamination by accidental ablation of adjacent titanite due to the small grain size, we consider this unlikely because 1) inclusions of titanite were not observed during BSE imaging on spots analysed by LA-ICP-MS, 2) all trace element analyses without exception (n = 20 for rutile, n = 10 for ilmenite) display similar and consistent REE concentrations (Fig. 4), and 3) measured Si and Fe concentrations do not indicate significant contamination (Table S4). Although REE concentrations in rutile and ilmenite are not commonly reported in the literature, some investigations of rutile from felsic systems show that, in some cases, rutile can incorporate these elements (Meyer et al., 2011; Ngo Bidjeck Bondje et al., 2020; Schirra and Laurent, 2021; Sciuba and Beaudoin, 2021). The similar REE concentrations and REE patterns between investigated rutile II, ilmenite and titanite (Fig. 4) suggest that these elements were immobile at a mineral scale during mineral reactions between these phases. Additionally, the systematic positive Eu anomaly in these minerals resembles the Eu anomaly reported in major minerals of the investigated samples such as vesuvianite and garnet (Butek et al., 2022). Therefore, we suggest that the prevailing Eu anomaly in minerals in Bôrček rodingites reflects

the destabilization and alteration of plagioclase, which was presumably the dominant mineral of the magmatic gabbroic protolith.

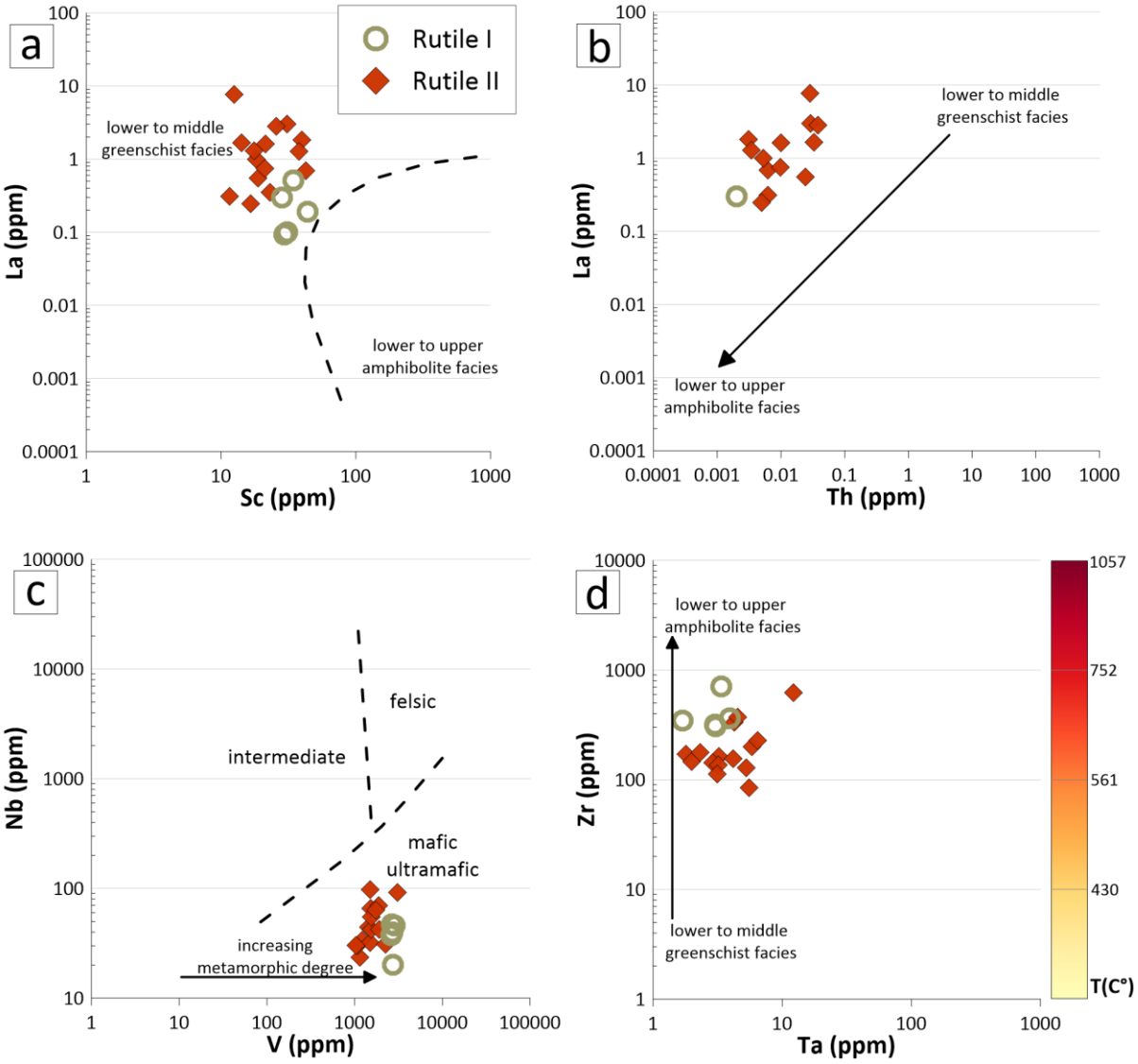

Fig. 7. *Selected trace element composition diagrams for the two types of rutile. a) La vs Sc. b) La vs Th. c) Nb vs V discrimination diagram consistent with the host mafic-ultramafic system. d) Zr vs Ta. The temperature bar was calculated according to the Zr-in-rutile thermometer (Ferry and Watson 2007) but it represents only maximum crystallization temperatures rather than absolute values due to the lack of reliable constraints on Zr and Si activities. The systematic differences between the two types of rutile suggest that rutile I formed at higher temperature than rutile II. All diagrams are adopted from Sciuba and Beaudoin (2021).*

The measured concentrations of V (1032 – 3088 ppm), Sb (5 – 570 ppm), and W (2 – 825 ppm) together with very low Nb (< 97 ppm) and Cr (< 313 ppm) in both types of investigated rutile are in good agreement with their metamorphic-hydrothermal origin in an ultramafic-mafic system (Meinhold et al., 2008; Sciuba and Beaudoin, 2021). Likewise, low HFSE concentrations in both rutile types (Fig. 5) are comparable with those reported from rutiles occurring in mafic lithologies (Miller et al., 2007; Zack et al., 2002; Zhao et al., 2017). An extensive review of rutile composition from various geological settings shows that the trace element concentration depends not only on the chemistry of the host

rock (ultramafic to felsic) but also on its metamorphic grade (Sciuba and Beaudoin, 2021). The difference in V concentration between rutile I and rutile II (2621 – 2851 ppm and 1032 – 2256 ppm, respectively) suggests that rutile I formed at higher metamorphic degree (upper greenschist facies) than rutile II (lower greenschist facies, Fig. 7a-c). This idea is also supported by significantly higher Hf concentration (> 10 ppm) and lower concentrations of REE (< 1 ppm) in rutile I than in rutile II, indicating again a higher metamorphic degree. Moreover, the difference in Zr concentration between rutile I (409 ppm in average) and rutile II (211 ppm in average, Fig. 5) is also consistent with the idea that rutile I formed at higher temperature than rutile II (Fig. 7d), despite the fact that due to lack of reliable constraints on Zr and Si activities, absolute Zr-in-rutile temperatures can not be reliably carried out (Ferry and Watson, 2007).

However, the lack of positive Eu anomaly in the majority of rutile I analyses and their low REE concentrations suggest that crystallization of rutile I occurred before the plagioclase breakdown. This would mean that this mineral predates the main rodingitization event (cf. Butek et al., 2022), such that the possibility of magmatic origin cannot be definitely ruled out. On the other hand, rutile forms almost exclusively during metamorphism and the magmatic origin of this mineral is relatively scarce (Force, 1980; Zack et al., 2002), especially in mafic magmas since Ti solubility increases with temperature and maficity (Ryerson and Watson, 1987). A notable exception is the occurrence of magmatic rutile in pyroxenite and chromitite cumulates (Zaccarini et al., 2021 and references therein), but such rutiles display much higher concentrations of Cr and V compared to rutile I from this study. In any case, geochemical data on magmatic rutiles from ultramafic-mafic systems are still scarce in the literature and definitive interpretation of the formation of rutile I thus remains challenging.

5.2 Mineral reactions and the origin of rutile II

Rutile I is both enclosed in ilmenite and crosscut by ilmenite veinlets (Fig. 3d, e). Despite the fact that ilmenite to rutile alteration has been observed starting in central parts of an ilmenite grain in an other context (Luvizotto et al., 2009), we interpret the texture in the sample FBR-57 as a feature of replacement of rutile by ilmenite. This is very similar to the metamorphic mineral succession rutile-ilmenite-titanite reported in an eclogitic body from Voltri ophiolite, Western Ligurian Alps (Liou et al., 1998). In this sense, ilmenite formed at least partially at the expense of rutile I. The iron required to this transformation can presumably come from the destabilization of primary (magmatic) pyroxenes.

Subsequently to this reaction, ilmenite and rutile were widely replaced by titanite. This reaction is commonly observed in metamorphic rocks (Angiboust and Harlov, 2017; Harlov et al., 2006; Pe-Piper et al., 2019) and can be expressed as:

$$2\ TiO_2\ (Rt\ I) + Si^{4+} + Ca^{2+} + 3\ O_2 \rightarrow 2\ CaTiSiO_5\ (Ttn) \qquad [1]$$

$$2\ FeTiO_3\ (Ilm) + 5\ Si^{4+} + 5\ Ca^{2+} + 8\ O_2 \rightarrow 2\ CaTiSiO_5\ (Ttn) + Ca_3Fe_2Si_3O_{12}\ (Adr) \qquad [2]$$

where the source of Si and Ca is the hydrothermal fluid dissolving primary Ca-silicates such as plagioclase in the case of an ultramafic-mafic system (Butek et al., 2022). The metamorphic origin of titanite is also indicated by its chemical composition characterized by high TiO_2 (> 36.5 wt.%) and low Al_2O_3 (< 1.3 wt.%) and FeO_{total} (< 0.7 wt.%), (Mohammad and Maekawa, 2008). Furthermore, the formation of andraditic garnet presumed from the reaction [2] is consistent with the titanite-andradite intergrowths observed in the investigated samples at the outer rim of the Fe-Ti rich aggregates (Fig. 3h).

The particular texture consisting of rutile II-calcite lamellae (Fig. 3b, d) and the widespread coexistence of these two minerals suggest their cogenetic origin. We interpret the lamellae texture as a form of exsolution resulting from destabillization of an earlier crystallized phase. Taking into account the chemical composition of the system (TiO_2-$CaCO_3$), a mineral able to supply Ti and Ca could be perovskite, $CaTiO_3$. Consequently, the following reaction is proposed:

$$CaTiO_3\ (Prv) + CO_2 \rightarrow TiO_2\ (Rt\ II) + CaCO_3\ (Cal) \quad [3]$$

where the source of CO_2 would be the hydrothermal fluid inducing the reaction. It is of note that perovskite was identified in some of the investigated samples. Although only as several tiny grains, it can be assumed that some of this phase remained unnoticed due to its small size and similar brightness in BSE imaging to that of rutile. Moreover, automorphic crystals of perovskite (up to 300 µm in size) were described in a reaction zone between rodingite and harzburgite at Dobšiná in the Western Carpathians (Li et al., 2014) and, similarly, perovskite was found in a rodingite-serpentinite reaction zone in China and Japan (Nishiyama et al., 2017; Shen et al., 2016). Therefore, perovskite occurrence in this type of hydrothermal rock would not be surprising. However, considering the molar volume of participating phases in the reaction [3], i.e. V_m (perovskite) = 34.7 cm^3/mol; V_m (rutile) = 18.8 cm^3/mol; V_m (calcite) = 36.9 cm^3/mol, we note that the perovskite destabilization would lead to a 160 % increase in volume. We thus consider the formation of the rutile-calcite lamellae texture by the destabilization of perovskite as unlikely.

As an alternative, we suggest that the formation of rutile II in association with calcite results from the destabilization of the first generation of titanite totally consumed by the following destabillization reaction:

$$CaTiSiO_5\ (Ttn\ I) + CO_2 \rightarrow TiO_2\ (Rt\ II) + CaCO_3\ (Cal) + Si^{4+} + O_2 \quad [4]$$

The source of CO_2 is associated with circulation of arc-related hydrothermal fluids, whereas silica and oxygen produced by the reaction would be leached out by the aqueous phase. The silica leaching and resulting absence of quartz as reaction product is not surprising as numerous studies show that desilication is an essential part of the rodingitization process (Butek et al., 2022; Duan et al., 2022; Rogkala et al., 2022). Above all, titanite is widespread in the investigated samples and such destabilization reaction is also well documented in the literature (e.g. Ault and Selverstone, 2008). Considering the molar volume of titanite (55.5 cm^3/mol) and the molar volume of the resulting 2-phase solid (18.8 + 36.9 = 55.7 cm^3/mol), we note that the titanite destabilization to form the rutile II + calcite association leads to virtually no volume change which makes this reaction highly probable as source of the observed texture. The P-T-X conditions for the reaction [4] were calculated using the Perple_X collection of programs, version 6.9.0 (Connolly, 2009; https://www.perplex.ethz.ch/), with the internally consistent thermodynamic database of Holland and Powell (1998). Equal molar amounts of CaO-TiO_2-SiO_2 and H_2O-CO_2 fluid defined by the state equation of CORK (Holland and Powell, 1991) were considered. The titanite destabilization into calcite and rutile is triggered mainly by decreasing temperature. The P-T conditions for this reaction are significantly dependent on the CO_2 concentration in the fluid (Fig. 8), with increasing $X(CO_2)$ leading to a shift of the titanite destabilization reaction towards higher temperatures. We thus suggest that the assumed first generation of titanite was destabilized by cooling during retrograde metamorphism, resulting into the formation of rutile II and calcite assemblage commonly featuring the particular lamellae, according to the reaction [4].

Since petrographic observations (Fig. 3b, c, d) indicate that titanite is the most recent mineral, we propose that this titanite represents the second titanite generation (Ttn II) whose crystallization could have been triggered by an influx of hydrothermal fluid with a higher O_2 fugacity (Henze et al., 2023 and references therein) during the final exhumation stage in which alteration occured under lower P-T conditions, according to the inverse reaction [4]:

$$TiO_2\ (Rt\ II) + CaCO_3\ (Cal) + Si^{4+} + O_2 \rightarrow CaTiSiO_5\ (Ttn\ II) + CO_2 \qquad [4']$$

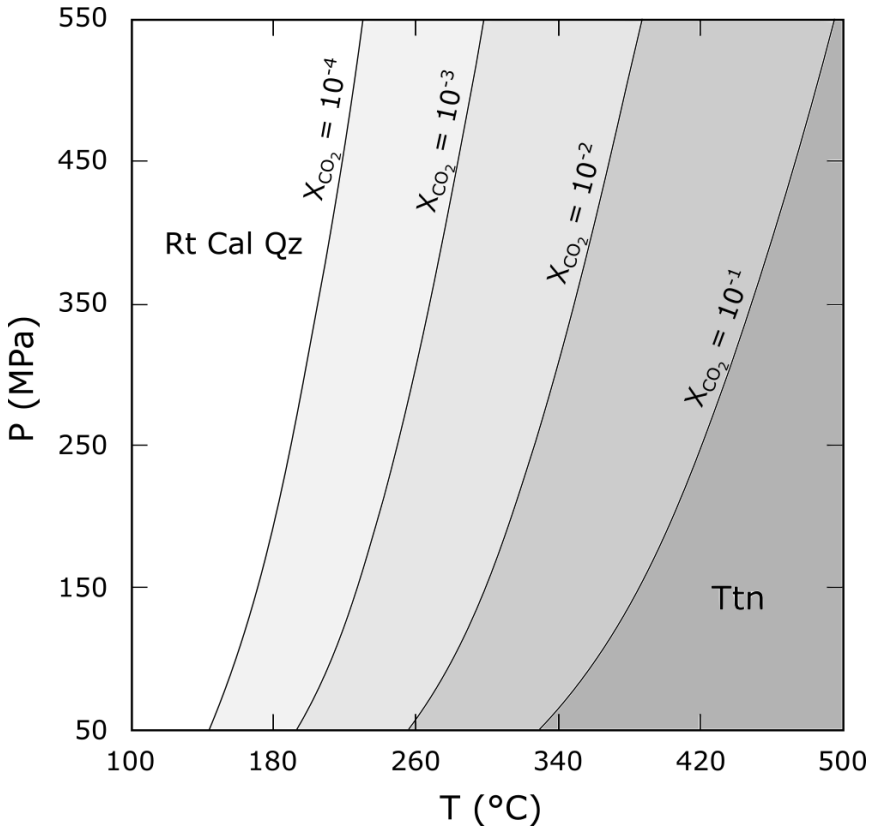

Fig. 8. *P-T diagram presenting the conditions for titanite (Ttn) to destabilize into rutile (Rt), calcite (Cal) and quartz (Qz) as calculated with Perple_X (Connolly 2009). Fluid saturated system consisting of equal molar amounts of CaO, TiO_2 and SiO_2 was used. Note the influence of CO_2 concentration in the fluid on the destabilization reaction. Perovskite is missing in the database (Holland and Powell 1998) and thus it is not included in the calculation.*

5.3 Age of alteration in context of the Western Carpathians

During the Triassic, the tectonic setting in the southern parts of the Western Carpathians was controlled by the rifting of the Meliata Ocean, which started at 243 Ma (Kozur, 1991; Plašienka, 2018). The age of the switch to the compressional regime and the onset of the Meliata subduction is not well constrained. The closure of the Meliata Ocean ended in the period between 160 – 150 Ma that corresponds to the age of peak blueschist facies metamorphism affecting the Meliaticum (Dallmeyer et al., 2008; Faryad and Henjes-Kunst, 1997). The following period is characterized by the tectonically complex formation of the Meliatic accretionary wedge (Putiš et al., 2019, 2014). Collision and thrusting of the Meliatic, Gemeric and Veporic units continued up to around 100 – 90 Ma when the deformation front progressively propagated into the northern parts of the Western Carpathians (Plašienka, 2018; Putiš et al., 2009). The alpine greenschist facies metamorphic imprint, which is widespread in the

Gemeric sequences, was constrained from $^{40}Ar/^{39}Ar$ dating of muscovite to the period between 142 and 87 Ma (Vozárová et al., 2005). $^{40}Ar/^{39}Ar$ whole-rock dating of phyllite from a Gemeric cover unit yielded a more precise age of 105.8 ± 1.5 Ma (Dallmeyer et al., 2008), which was also recently confirmed by extensive dating of monazite from phyllites of the Meliatic unit (Potočný et al., 2020). Moreover, a U-Pb SIMS dating of metamorphic rutile in a metabasalt from the Meliaticum yielded an age of 100 ± 10 Ma (Putiš et al., 2019). The U-Pb dating of rutile II in the Bôrček rodingites (this study) indicates that it crystallized at 102.6 ± 19.9 Ma, which is within uncertainty identical to the later stages of the alpine greenschist-facies regional metamorphism published in the literature (Fig. 9).

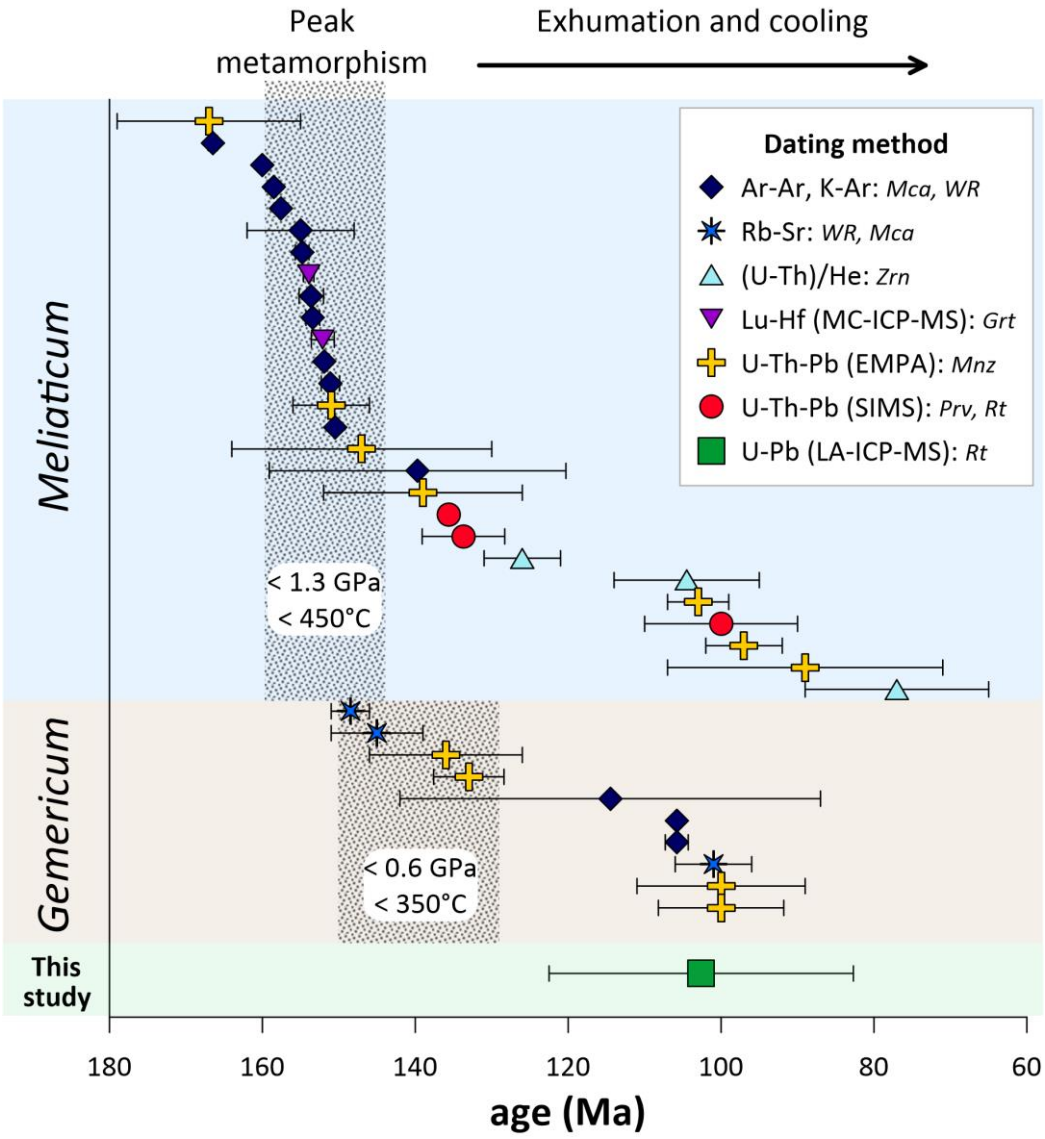

Fig. 9. *Compilation of metamorphic ages related to the Alpine orogenesis in the southern parts of the Western Carpathians. Complete reference list is available in the Table S6). Indicated peak metamorphic conditions are adopted from Faryad et al. (2020). The age reported in this study is consistent with other data and indicates that rutile II formed during the exhumation of the accretionary wedge. Mineral abbreviations (in italic) are after Warr (2021), WR – whole rock.*

Until present, the only information on the timing of serpentinization and rodingitization processes in the Western Carpathians has been obtained from a U-Pb SIMS dating of perovskite from a serpentinite body at Dobšiná (Li et al., 2014). The serpentinite occurrence is assigned to the Meliaticum.

Idiomorphic perovskite crystals were found in a reaction zone between serpentinized harzburgite and rodingite. The dating yielded ages of 135.6 ± 0.58 Ma and 133.7 ± 5.4 Ma that are significantly older than our ages for the Bôrček occurrence but still in accordance with the period of formation of the Meliatic accretionary wedge and associated regional metamorphism (Fig. 9) (cf. Plašienka, 2018). The discrepancy can be attributed either to a slightly different tectonic and metamorphic evolution of the considered serpentinite bodies, or to the fact that rutile II dated in this study could have formed later than the chronologically constrained perovskite in regard of the ongoing serpentinization process.

5.4 Geodynamic setting of the rodingitization process

The obtained chemical and chronological data allow to discuss the geodynamic setting of formation of the rodingites from Bôrček. Despite the fact that the origin of the serpentinite body is still not clear, based on its actual tectonic position within the Gemeric cover metasedimentary sequence, we can assume that its geodynamic evolution during the late alpine orogenesis is similar to the evolution of the Gemericum (Fig. 9). Our new dating result for the crystallization of rutile II at 102.6 ± 19.9 Ma places the formation of this mineral to the retrograde metamorphism in a greenschist facies environment associated with cooling. This is consistent with the inferred reaction responsible for the formation of rutile II + calcite through retrograde breakdown of titanite owing to the cooling, silica leaching and influx of CO_2-rich fluids [4], induced by progressive exhumation of the investigated rocks.

Butek et al. (2022) have identified two stages of the rodingitization process. The first one was characterized by the formation of main rodingite minerals such as vesuvianite, diopside and garnet, while veins of vesuvianite and garnet and the aggregates of Fe-Ti minerals including rutile II formed during the second stage of rodingitization. Following these more or less continuous events, the investigated rocks were affected by the formation of an epidote-chlorite-calcite assemblage, which has been interpreted to result from the alpine regional metamorphism at greenschist facies conditions (Butek et al., 2022). Considering the petrochronological results of this work, we conclude that both the second stage of rodingitization and the late hydrothermal alteration (inducing the formation of epidote, chlorite and calcite) took place during the exhumation at later stages of the alpine (Cretaceous) geotectonic evolution. However, such interpretation naturally questions the origin of the shift from the mineralogy typical for rodingites (vesuvianite, garnet) to the formation of minerals typical for greenschist facies metamorphism such as epidote and chlorite. Decreasing temperature could eventually represent a key factor, however, rodingites can form at low P-T sub-greenschist facies conditions as well (Dubińska et al., 2004; Schandl et al., 1989). On the other hand, hydrothermal fluid, compositionally buffered by an ultramafic lithology, is indispensable to the formation of rodingites (Bach and Klein, 2009; Palandri and Reed, 2004). For this reason, we rather propose that the rodingitization process was interrupted by dismembering of a larger ultramafic body. Dismembering could induce a change in chemistry of the fluid circulating in the system, which led to the crystallization of a more common greenschist facies metamorphic assemblage consisting predominantly of epidote and chlorite.

The investigated rodingite samples do not display any record of hydrothermal alteration occurring in ocean floor environment before the onset of subduction. If any, it has been fully overprinted during the following geotectonic evolution. The alpine subduction-collision-obduction activity caused the ultramafic body to undergo metamorphic and hydrothermal alteration processes that have led to the formation of rodingites at Bôrček. The determined crystallization age of rutile II indicates that this mineral formed during exhumation (Fig. 9) and petrographic observations suggest that its

crystallization was triggered during the rodingitization process. The first stage of rodingitization reported by Butek et al. (2022) could have taken place virtually at any place in the subduction environment at any P-T conditions along the assumed P-T path. Despite that, we show that the detailed petrographical, geochemical and geochronological investigation allows to place the second stage of rodingitization (and the simultaneous serpentinization) in the greenschist facies environment of the exhuming Meliatic accretionary wedge.

6 Conclusions

- Fe-Ti rich aggregates in rodingites from the Bôrček serpentinite body consist mainly of ilmenite, titanite, calcite and two distinct generations of rutile (rutile I and II).
- All investigated minerals display low HFSE concentration in accordance with the ultramafic-mafic nature of the system. These Fe-Ti minerals (except rutile I) also display significant REE concentrations and pronounced positive Eu anomalies. Plagioclases from the gabbroic protolith are interpreted as the source of this prevailing Eu anomaly. Moreover, the similarity of REE patterns between the investigated phases suggests that the REE concentrations in Fe-Ti minerals are controlled by the immobility and availability of these elements in the system.
- Textural relationships and chemical compositions of the investigated Ti-minerals suggest their hydrothermal-metamorphic origin, although rutile I could eventually be of the magmatic origin. In any case, rutile I formed at higher temperature than rutile II.
- Rutile II (together with the particular rutile II – calcite lamellae texture) originated from the titanite destabilization, which was triggered by cooling, silica leaching and influx of CO_2-rich fluids. The occurrence of the rutile II – calcite assemblage indicates a pre-existing titanite generation in the mineral evolution of the investigated rodingites.
- In situ U-Pb dating of rutile II yielded a crystallization age of 102.6 ± 19.9 Ma. This age is consistent with the retrograde stage of the alpine tectono-metamorphic evolution of the Western Carpathians in the Cretaceous. This suggests that at least a part of rodingitization (and serpentinization) process took place during the exhumation and cooling of the accretionary wedge resulting from the closure of the Meliata Ocean.

Acknowledgements

We thank two anonymous reviewers for their constructive comments which substantially improved the final version of the manuscript. We also thank Tomáš Mikuš for his assistance during electron microscopy and microprobe analysis. This research was funded by the TelluS Program of CNRS/INSU and the Slovak Research and Development Agency (APVV 19-0065).

References

Angiboust, S., Harlov, D., 2017. Ilmenite breakdown and rutile-titanite stability in metagranitoids: Natural observations and experimental results. Am. Mineral. 102, 1696–1708. https://doi.org/10.2138/am-2017-6064

Ault, A.K., Selverstone, J., 2008. Microtextural constraints on the interplay between fluid–rock reactions and deformation. Contrib. Mineral. Petrol. 156, 501–515. https://doi.org/10.1007/s00410-008-0298-9

Bach, W., Klein, F., 2009. The petrology of seafloor rodingites: Insights from geochemical reaction path modeling. Lithos 112, 103–117. https://doi.org/10.1016/j.lithos.2008.10.022

Broska, I., Harlov, D., Tropper, P., Siman, P., 2007. Formation of magmatic titanite and titanite–ilmenite phase relations during granite alteration in the Tribeč Mountains, Western Carpathians, Slovakia. Lithos 95, 58–71. https://doi.org/10.1016/j.lithos.2006.07.012

Butek, J., Grégoire, M., Spišiak, J., Duchene, S., Kopáčik, R., 2022. On the origin of vesuvianite-rich rodingites from the Western Carpathians, Slovakia. Lithos 432–433, 106902. https://doi.org/10.1016/j.lithos.2022.106902

Butek, J., Spišiak, J., Milovská, S., 2021. Garnet-Vesuvianite Equilibrium in Rodingites from Dobšiná (Western Carpathians). Minerals 11, 189. https://doi.org/10.3390/min11020189

Connolly, J. a. D., 2009. The geodynamic equation of state: What and how. Geochem. Geophys. Geosystems 10. https://doi.org/10.1029/2009GC002540

Dallmeyer, R.D., Neubauer, F., Fritz, H., 2008. The Meliata suture in the Carpathians: regional significance and implications for the evolution of high-pressure wedges within collisional orogens. Geol. Soc. Lond. Spec. Publ. 298, 101–115. https://doi.org/10.1144/SP298.6

Duan, W.-Y., Li, X.-P., Schertl, H.-P., Willner, A.P., Wang, S.-J., Chen, S., Sun, G.-M., 2022. Rodingitization records from ocean-floor to high pressure metamorphism in the Xigaze ophiolite, southern Tibet. Gondwana Res., Metamorphism and Magmatism of the Tibetan Plateau and Tethys evolution 104, 126–153. https://doi.org/10.1016/j.gr.2021.05.013

Dubińska, E., Bylina, P., Kozłowski, A., Dörr, W., Nejbert, K., Schastok, J., Kulicki, C., 2004. U–Pb dating of serpentinization: hydrothermal zircon from a metasomatic rodingite shell (Sudetic ophiolite, SW Poland). Chem. Geol. 203, 183–203. https://doi.org/10.1016/j.chemgeo.2003.10.005

Faryad, S.W., Henjes-Kunst, F., 1997. Petrological and KAr and40Ar39Ar age constraints for the tectonothermal evolution of the high-pressure Meliata unit, Western Carpathians (Slovakia). Tectonophysics, Thermal and Mechanical Interactions in Deep-Seated Rocks 280, 141–156. https://doi.org/10.1016/S0040-1951(97)00141-8

Faryad, S.W., Ivan, P., Jedlicka, R., 2020. Pre-Alpine high-pressure metamorphism in the Gemer unit: mineral textures and their geodynamic implications for Variscan Orogeny in the Western Carpathians. Int. J. Earth Sci. 109, 1547–1564. https://doi.org/10.1007/s00531-020-01856-2

Ferry, J.M., Watson, E.B., 2007. New thermodynamic models and revised calibrations for the Ti-in-zircon and Zr-in-rutile thermometers. Contrib. Mineral. Petrol. 154, 429–437. https://doi.org/10.1007/s00410-007-0201-0

Force, E.R., 1980. The Provenance of Rutile. J. Sediment. Res. Vol. 50, 485–488. https://doi.org/10.1306/212F7A31-2B24-11D7-8648000102C1865D

Geologická mapa Slovenska M 1:50 000 [online]. Bratislava: Štátny geologický ústav Dionýza Štúra. [WWW Document], 2013. . http://apl.geology.sk/gm50js.

Griffin, W.L., Powell, W.J., Pearson, N.J., O'Reilly, S.Y., 2008. GLITTER : Data reduction software for laser ablation ICP-MS, in: Laser Ablation ICP-MS in the Earth Sciences : Current Practices and Outstanding Issues, Short Course (Book 40). Mineralogical Association of Canada, Vancouver, pp. 308–311.

Harlov, D., Tropper, P., Seifert, W., Nijland, T., Förster, H.-J., 2006. Formation of Al-rich titanite (CaTiSiO4O–CaAlSiO4OH) reaction rims on ilmenite in metamorphic rocks as a function of fH2O and fO2. Lithos 88, 72–84. https://doi.org/10.1016/j.lithos.2005.08.005

Haws, A.A., Starr, P.G., Dragovic, B., Scambelluri, M., Belmonte, D., Caddick, M.J., Broadwell, K.S., Ague, J.J., Baxter, E.F., 2021. Meta-rodingite dikes as recorders of subduction zone metamorphism and serpentinite dehydration: Voltri Ophiolite, Italy. Chem. Geol. 565, 120077. https://doi.org/10.1016/j.chemgeo.2021.120077

Hellstrom, J., Paton, C., Woodhead, J., Hergt, J., 2008. Iolite: software for spatially resolved LA-(quad and MC)-ICP-MS analysis, in: Laser Ablation ICP-MS in the Earth Sciences : Current practices and outstanding issues, Short Course (Book 40). Mineralogical Association of Canada, Vancouver, pp. 343–348.

Henze, P.K., Christiansen, E.H., Kowallis, B.J., Dorais, M.J., Mosher, H.D., Franzen, L.M., Martin, A.J., Nabelek, P.I., 2023. Titanite geochemistry and textures: Implications for magmatic and post-magmatic processes in the Notch Peak and Little Cottonwood granitic intrusions, Utah. Am. Mineral. 108, 226–248. https://doi.org/10.2138/am-2022-8241

Holland, T., Powell, R., 1991. A Compensated-Redlich-Kwong (CORK) equation for volumes and fugacities of CO2 and H2O in the range 1 bar to 50 kbar and 100–1600°C. Contrib. Mineral. Petrol. 109, 265–273. https://doi.org/10.1007/BF00306484

Holland, T.J.B., Powell, R., 1998. An internally consistent thermodynamic data set for phases of petrological interest. J. Metamorph. Geol. 16, 309–343. https://doi.org/10.1111/j.1525-1314.1998.00140.x

Honnorez, J., Kirst, P., 1975. Petrology of rodingites from the equatorial Mid-Atlantic fracture zones and their geotectonic significance. Contrib. Mineral. Petrol. 49, 233–257. https://doi.org/10.1007/BF00376590

Hovorka, D., Dubíková, K., Gerthofferová, H., Šamajová, E., Turan, J., 1983. Serpentine-group minerals of the West Carpathian ultramafics. II -Bodies in Pre-Mesozoic metamorphosed complexes.pdf. Miner. Slovaca 15, 23–47.

Hovorka, D., Dubíková, K., Gerthofferová, H., Šamajová, E., Turan, J., 1980. Serpentine-group minerals of the Western Carpathians ultramafics. I – Bodies of the Gemeride Mesozoic. Miner. Slovaca 12, 481–505.

Hovorka, D., Ivan, P., Jaroš, J., Kratochvíl, M., Reichwalder, P., Rojkovič, I., Spišiak, J., Turanová, L., 1985. Ultramafic Rocks of the Western Carpathians / Czechoslovakia. GÚDŠ, Bratislava.

Hovorka, D., Ivan, P., Spišiak, J., 1990. Lithology, petrology, metamorphism and tectonic position of the Klátov group (paleozoic of the Gemer unit, Inner Western Carpathians). Acta Geol. Geogr. Univ. Comen. Geol. 55–69.

Hu, C.-N., Santosh, M., 2018. Devonian rodingite from the northern margin of the North China Craton: mantle wedge metasomatism during ocean-continent convergence. Int. Geol. Rev. 60, 1073–1097. https://doi.org/10.1080/00206814.2017.1365631

Ivan, P., 2002. Relics of Meliata ocean crust: geodynamic implications of mineralogical, petrological and geochemical proxies. Geol. Carpathica 53, 254–256.

Janssen, A., Putnis, A., Geisler, T., Putnis, C.V., 2010. The experimental replacement of ilmenite by rutile in HCl solutions. Mineral. Mag. 74, 633–644. https://doi.org/10.1180/minmag.2010.074.4.633

Jochum, K.P., Weis, U., Stoll, B., Kuzmin, D., Yang, Q., Raczek, I., Jacob, D.E., Stracke, A., Birbaum, K., Frick, D.A., Günther, D., Enzweiler, J., 2011. Determination of Reference Values for NIST SRM 610–617 Glasses Following ISO Guidelines. Geostand. Geoanalytical Res. 35, 397–429. https://doi.org/10.1111/j.1751-908X.2011.00120.x

Koutsovitis, P., 2017. High-pressure subduction-related serpentinites and metarodingites from East Thessaly (Greece): Implications for their metamorphic, geochemical and geodynamic evolution in the Hellenic–Dinaric ophiolite context. Lithos, European Lithospheric Mantle; geochemical, petrological and geophysical processes 276, 122–145. https://doi.org/10.1016/j.lithos.2016.11.008

Koutsovitis, P., Magganas, A., Ntaflos, T., Koukouzas, N., 2018. Rodingitization and carbonation, associated with serpentinization of Triassic ultramafic cumulates and lavas in Othris, Greece. Lithos 320–321, 35–48. https://doi.org/10.1016/j.lithos.2018.08.027

Koutsovitis, P., Magganas, A., Pomonis, P., Ntaflos, T., 2013. Subduction-related rodingites from East Othris, Greece: Mineral reactions and physicochemical conditions of formation. Lithos 172–173, 139–157. https://doi.org/10.1016/j.lithos.2013.04.009

Kozur, H., 1991. The evolution of the Meliata-Hallstatt ocean and its significance for the early evolution of the Eastern Alps and Western Carpathians. Palaeogeogr. Palaeoclimatol. Palaeoecol. 87, 109–135. https://doi.org/10.1016/0031-0182(91)90132-B

Laborda-López, C., López-Sánchez-Vizcaíno, V., Marchesi, C., Gómez-Pugnaire, M.T., Garrido, C.J., Jabaloy-Sánchez, A., Padrón-Navarta, J.A., Hidas, K., 2018. High- *P* metamorphism of rodingites during serpentinite dehydration (Cerro del Almirez, Southern Spain): Implications for the redox state in subduction zones. J. Metamorph. Geol. 36, 1141–1173. https://doi.org/10.1111/jmg.12440

Li, X.-H., Putiš, M., Yang, Y.-H., Koppa, M., Dyda, M., 2014. Accretionary wedge harzburgite serpentinization and rodingitization constrained by perovskite U/Pb SIMS age, trace elements and Sm/Nd isotopes: Case study from the Western Carpathians, Slovakia. Lithos 205, 1–14. https://doi.org/10.1016/j.lithos.2014.06.001

Li, X.-P., Duan, W.-Y., Zhao, L.-Q., Schertl, H.-P., Kong, F.-M., Shi, T.-Q., Zhang, X., 2017. Rodingites from the Xigaze ophiolite, southern Tibet – new insights into the processes of rodingitization. Eur. J. Mineral. 29, 821–837. https://doi.org/10.1127/ejm/2017/0029-2633

Li, X.-P., Rahn, M., Bucher, K., 2004. Metamorphic Processes in Rodingites of the Zermatt-Saas Ophiolites. Int. Geol. Rev. 46, 28–51. https://doi.org/10.2747/0020-6814.46.1.28

Li, X.-P., Zhang, L., Wei, C., Ai, Y., Chen, J., 2007. Petrology of rodingite derived from eclogite in western Tianshan, China. J. Metamorph. Geol. 25, 363–382. https://doi.org/10.1111/j.1525-1314.2007.00700.x

Li, X.-P., Zhang, L.-F., Wilde, S.A., Song, B., Liu, X.-M., 2010. Zircons from rodingite in the Western Tianshan serpentinite complex: Mineral chemistry and U–Pb ages define nature and timing of rodingitization. Lithos 118, 17–34. https://doi.org/10.1016/j.lithos.2010.03.009

Liou, J.G., Zhang, R., Ernst, W.G., 1998. Mineral parageneses in the Piampaludo eclogitic body, Gruppo di Voltri, Western Ligurian Alps. https://doi.org/10.5169/SEALS-59291

Lucassen, F., Franz, G., Wirth, R., Weise, M., Hertwig, A., 2012. The morphology of the reaction front of the dissolution-precipitation reaction rutile + wollastonite = titanite in time series experiments at 600 C/400 MPa. Am. Mineral. 97, 828–839. https://doi.org/10.2138/am.2012.3742

Luvizotto, G.L., Zack, T., Meyer, H.P., Ludwig, T., Triebold, S., Kronz, A., Münker, C., Stockli, D.F., Prowatke, S., Klemme, S., Jacob, D.E., von Eynatten, H., 2009. Rutile crystals as potential trace element and isotope mineral standards for microanalysis. Chem. Geol. 261, 346–369. https://doi.org/10.1016/j.chemgeo.2008.04.012

Luvizotto, G.L., Zack, T., Triebold, S., von Eynatten, H., 2009. Rutile occurrence and trace element behavior in medium-grade metasedimentary rocks: example from the Erzgebirge, Germany. Mineral. Petrol. 97, 233–249. https://doi.org/10.1007/s00710-009-0092-z

McDonough, W.F., Sun, S. -s., 1995. The composition of the Earth. Chem. Geol. 120, 223–253.

Meinhold, G., Anders, B., Kostopoulos, D., Reischmann, T., 2008. Rutile chemistry and thermometry as provenance indicator: An example from Chios Island, Greece. Sediment. Geol. 203, 98–111. https://doi.org/10.1016/j.sedgeo.2007.11.004

Meyer, M., John, T., Brandt, S., Klemd, R., 2011. Trace element composition of rutile and the application of Zr-in-rutile thermometry to UHT metamorphism (Epupa Complex, NW Namibia). Lithos 126, 388–401. https://doi.org/10.1016/j.lithos.2011.07.013

Miller, C., Zanetti, A., Thöni, M., Konzett, J., 2007. Eclogitisation of gabbroic rocks: Redistribution of trace elements and Zr in rutile thermometry in an Eo-Alpine subduction zone (Eastern Alps). Chem. Geol. 239, 96–123. https://doi.org/10.1016/j.chemgeo.2007.01.001

Mohammad, Y.O., Maekawa, H., 2008. Origin of titanite in metarodingite from the Zagros Thrust Zone, Iraq. Am. Mineral. 93, 1133–1141. https://doi.org/10.2138/am.2008.2580

Ngo Bidjeck Bondje, L.M., Bineli Betsi, T., Mama Nga, L.N.Y., Ngo Belnoun, R.N., Molotouala, A.C., McFarlane, C., Bitom, L.D., 2020. Geochemistry of rutile from the Pan-African Yaoundé metamorphic group: Implications for provenance and conditions of formation. J. Afr. Earth Sci. 170, 103912. https://doi.org/10.1016/j.jafrearsci.2020.103912

Nishiyama, T., Yoshida-Shiosaki, C., Mori, Y., Shigeno, M., 2017. Interplay of irreversible reactions and deformation: a case of hydrofracturing in the rodingite-serpentinite system. Prog. Earth Planet. Sci. 4, UNSP 1. https://doi.org/10.1186/s40645-016-0115-4

Palandri, J.L., Reed, M.H., 2004. Geochemical models of metasomatism in ultramafic systems: serpentinization, rodingitization, and sea floor carbonate chimney precipitation. Geochim. Cosmochim. Acta 68, 1115–1133. https://doi.org/10.1016/j.gca.2003.08.006

Paton, C., Woodhead, J.D., Hellstrom, J.C., Hergt, J.M., Greig, A., Maas, R., 2010. Improved laser ablation U-Pb zircon geochronology through robust downhole fractionation correction. Geochem. Geophys. Geosystems 11. https://doi.org/10.1029/2009GC002618

Pe-Piper, G., Nagle, J., Piper, D.J.W., McFarlane, C.R.M., 2019. Geochronology and trace element mobility in rutile from a Carboniferous syenite pegmatite and the role of halogens. Am. Mineral. 104, 501–513. https://doi.org/10.2138/am-2019-6668

Petrus, J.A., Kamber, B.S., 2012. VizualAge: A Novel Approach to Laser Ablation ICP-MS U-Pb Geochronology Data Reduction. Geostand. Geoanalytical Res. 36, 247–270. https://doi.org/10.1111/j.1751-908X.2012.00158.x

Plašienka, D., 2018. Continuity and Episodicity in the Early Alpine Tectonic Evolution of the Western Carpathians: How Large-Scale Processes Are Expressed by the Orogenic Architecture and Rock Record Data. Tectonics 37, 2029–2079. https://doi.org/10.1029/2017TC004779

Plašienka, D., Méres, Š., Ivan, P., Sýkora, M., Soták, J., Lačný, A., Aubrecht, R., Bellová, S., Potočný, T., 2019. Meliatic blueschists and their detritus in Cretaceous sediments: new data constraining tectonic evolution of the West Carpathians. Swiss J. Geosci. 112, 55–81. https://doi.org/10.1007/s00015-018-0330-7

Pomonis, P., Tsikouras, B., Karipi, S., Hatzipanagiotou, K., 2008. Rodingite formation in ultramafic rocks from the Koziakas ophiolite, western Thessaly, Greece: Conditions of metasomatic alteration, geochemical exchanges and T-X(CO2) evolutionary path. Can. Mineral. 46, 569–581. https://doi.org/10.3749/canmin.46.3.569

Potočný, T., Méres, Š., Plašienka, D., 2020. Geological structure and tectonometamorphic evolution of the Veporic–Gemeric contact zone constrained by the monazite age data (Slavošovce–Štítnik area, Western Carpathians, Slovakia). Miner. Slovaca 52, 83–102.

Putiš, M., Danišík, M., Ružička, P., Schmiedt, I., 2014. Constraining exhumation pathway in an accretionary wedge by (U-Th)/He thermochronology—Case study on Meliatic nappes in the Western Carpathians. J. Geodyn. 81, 80–90. https://doi.org/10.1016/j.jog.2014.07.009

Putiš, M., Frank, W., Plašienka, D., Siman, P., Sulák, M., Biron, A., 2009. Progradation of the Alpidic Central Western Carpathians orogenic wedge related to two subductions: constrained by ^{40}Ar/ ^{39}Ar ages of white micas. Geodin. Acta 22, 31–56. https://doi.org/10.3166/ga.22.31-56

Putiš, Soták, Li, Ondrejka, Li, Hu, Ling, Nemec, Németh, Ružička, 2019. Origin and Age Determination of the Neotethys Meliata Basin Ophiolite Fragments in the Late Jurassic–Early Cretaceous Accretionary Wedge Mélange (Inner Western Carpathians, Slovakia). Minerals 9, 652. https://doi.org/10.3390/min9110652

Radvanec, M., Németh, Z., Kráľ, J., Pramuka, S., 2017. Variscan dismembered metaophiolite suite fragments of Paleo-Tethys in Gemeric unit, Western Carpathians. Miner. Slovaca 49, 1–48.

Rogkala, A., Petrounias, P., Koutsovitis, P., Giannakopoulou, P.P., Pomonis, P., Lampropoulou, P., Hatzipanagiotou, K., 2022. Rodingites from the Veria-Naousa ophiolite (Greece): Mineralogical evolution, metasomatism and petrogenetic processes. Geochemistry 125860. https://doi.org/10.1016/j.chemer.2021.125860

Ryerson, F.J., Watson, E.B., 1987. Rutile saturation in magmas: implications for Ti-Nb-Ta depletion in island-arc basalts. Earth Planet. Sci. Lett. 86, 225–239.

Schandl, E.S., O'Hanley, D.S., Wicks, F.J., 1989. Rodingites in serpentinized ultramafic rocks of the Abitibi Greenstone belt, Ontario. Can. Mineral. 27, 579–591.

Schirra, M., Laurent, O., 2021. Petrochronology of hydrothermal rutile in mineralized porphyry Cu systems. Chem. Geol. 581, 120407. https://doi.org/10.1016/j.chemgeo.2021.120407

Schmitt, A.K., Zack, T., 2012. High-sensitivity U–Pb rutile dating by secondary ion mass spectrometry (SIMS) with an O2+ primary beam. Chem. Geol. 332–333, 65–73. https://doi.org/10.1016/j.chemgeo.2012.09.023

Schwartz, S., Gautheron, C., Ketcham, R.A., Brunet, F., Corre, M., Agranier, A., Pinna-Jamme, R., Haurine, F., Monvoin, G., Riel, N., 2020. Unraveling the exhumation history of high-pressure ophiolites using magnetite (U-Th-Sm)/He thermochronometry. Earth Planet. Sci. Lett. 543, 116359. https://doi.org/10.1016/j.epsl.2020.116359

Sciuba, M., Beaudoin, G., 2021. Texture and Trace Element Composition of Rutile in Orogenic Gold Deposits. Econ. Geol. 116, 1865–1892. https://doi.org/10.5382/econgeo.4857

Shen, T., Wu, F., Zhang, L., Hermann, J., Li, X., Du, J., 2016. In-situ U–Pb dating and Nd isotopic analysis of perovskite from a rodingite blackwall associated with UHP serpentinite from southwestern Tianshan, China. Chem. Geol. 431, 67–82. https://doi.org/10.1016/j.chemgeo.2016.03.029

Stacey, J.S., Kramers, J.D., 1975. Approximation of terrestrial lead isotope evolution by a two-stage model. Earth Planet. Sci. Lett. 26, 207–221. https://doi.org/10.1016/0012-821X(75)90088-6

Tang, Y., Zhai, Q.-G., Hu, P.-Y., Wang, J., Xiao, X.-C., Wang, H.-T., Tang, S.-H., Lei, M., 2018. Rodingite from the Beila ophiolite in the Bangong–Nujiang suture zone, northern Tibet: New insights into the formation ofophiolite-related rodingite. Lithos 316–317, 33–47. https://doi.org/10.1016/j.lithos.2018.07.006

Vermeesch, P., 2018. IsoplotR: A free and open toolbox for geochronology. Geosci. Front., SPECIAL ISSUE: Frontiers in geoscience:A tribute to Prof. Xuanxue Mo 9, 1479–1493. https://doi.org/10.1016/j.gsf.2018.04.001

Vozárová, A., Frank, W., Kráľ, J., Vozár, J., 2005. 40Ar/39Ar dating of detrital mica from the Upper Paleozoic sandstones in the Western Carpathians (Slovakia). Geol. Carpathica 56, 463–472.

Warr, L.N., 2021. IMA–CNMNC approved mineral symbols. Mineral. Mag. 85, 291–320. https://doi.org/10.1180/mgm.2021.43

Zaccarini, F., Garuti, G., Luvizotto, G.L., de Melo Portella, Y., Singh, A.K., 2021. Testing Trace-Element Distribution and the Zr-Based Thermometry of Accessory Rutile from Chromitite. Minerals 11, 661. https://doi.org/10.3390/min11070661

Zack, T., Kronz, A., Foley, S.F., Rivers, T., 2002. Trace element abundances in rutiles from eclogites and associated garnet mica schists. Chem. Geol. 184, 97–122. https://doi.org/10.1016/S0009-2541(01)00357-6

Zhao, L.H., Zeng, L.S., Hu, M.Y., Sun, D.Y., 2017. Rutile to titanite transformation in amphibolite and its geochemical consequences: A case study of the amphibolite from Yarlung Tsangpo suture zone. Yanshi XuebaoActa Petrol. Sin. 33, 2494–2508.